



HAL
open science

Multi-method dating reveals 200 ka of Middle Palaeolithic occupation at Maras rock shelter, Rhône Valley, France

Mailys Richard, Miren del Val, Helen Fewlass, Virginie Sinet-Mathiot, Philippe Lanos, Edwige Pons-Branchu, Simon Puaud, Jean-Jacques Hublin, Marie-Hélène Moncel

► **To cite this version:**

Mailys Richard, Miren del Val, Helen Fewlass, Virginie Sinet-Mathiot, Philippe Lanos, et al.. Multi-method dating reveals 200 ka of Middle Palaeolithic occupation at Maras rock shelter, Rhône Valley, France. *Scientific Reports*, 2024, 14 (1), pp.20474. 10.1038/s41598-024-69380-w . hal-04687247

HAL Id: hal-04687247

<https://hal.science/hal-04687247>

Submitted on 4 Sep 2024

HAL is a multi-disciplinary open access archive for the deposit and dissemination of scientific research documents, whether they are published or not. The documents may come from teaching and research institutions in France or abroad, or from public or private research centers.

L'archive ouverte pluridisciplinaire **HAL**, est destinée au dépôt et à la diffusion de documents scientifiques de niveau recherche, publiés ou non, émanant des établissements d'enseignement et de recherche français ou étrangers, des laboratoires publics ou privés.



OPEN

Multi-method dating reveals 200 ka of Middle Palaeolithic occupation at Maras rock shelter, Rhône Valley, France

Maïlys Richard^{1,2,3,✉}, Miren del Val², Helen Fewlass^{4,5}, Virginie Sinet-Mathiot^{4,6,7}, Philippe Lanos^{1,12}, Edwige Pons-Branchu⁸, Simon Puaud⁹, Jean-Jacques Hublin^{4,10} & Marie-Hélène Moncel¹¹

The emergence of the Middle Palaeolithic, and its variability over time and space are key questions in the field of prehistoric archaeology. Many sites have been documented in the south-eastern margins of the Massif central and the middle Rhône valley, a migration path that connects Northern Europe with the Mediterranean. Well-dated, long stratigraphic sequences are essential to understand Neanderthals dynamics and demise, and potential interactions with *Homo sapiens* in the area, such as the one displayed at the Maras rock shelter ("Abri du Maras"). The site is characterised by exceptional preservation of archaeological remains, including bones dated using radiocarbon (¹⁴C) and teeth using electron spin resonance combined with uranium series (ESR/U-series). Optically stimulated luminescence was used to date the sedimentary deposits. By combining the new ages with previous ones using Bayesian modelling, we are able to clarify the occupation time over a period spanning 200,000 years. Between ca. 250 and 40 ka, the site has been used as a long-term residence by Neanderthals, specifically during three interglacial periods: first during marine isotopic stage (MIS) 7, between 247 ± 34 and 223 ± 33 ka, and then recurrently during MIS 5 (between 127 ± 17 and 90 ± 9 ka) and MIS 3 (up to 39,280 cal BP).

Keywords Chronology, Neanderthal, Luminescence, Radiocarbon, Electron spin resonance, Uranium-series, Bayesian modelling, ZooMS

In south-eastern France, the Rhodanian corridor, which connects the North of Europe and the Mediterranean basin, has been a hotspot for human occupation and used as a migration path starting from the Middle Pleistocene. In particular, in the middle Rhône valley and the south-eastern margins of the Massif central, the earliest evidence of Levallois technology has been documented ca. 300 ka years ago in Orgnac^{1,2} and in Payre³⁻⁵ (Fig. 1).

The density of sites increased during the Late Pleistocene, where Neanderthal sites are mainly dated to marine isotopic stage (MIS) 5 to 3 (e.g.,^{5,6}) and *Homo sapiens* may have been present as early as ca. 54 ka⁷. The earliest evidence of Aurignacian cave art in France is documented at the Chauvet cave, ca. 36 ka (e.g.,^{8,9}). In this context, the chronology of the Maras rock shelter is essential for our understanding of population dynamics during this period, considering that Neanderthals and *Homo sapiens* may have crossed paths in this area.

¹Archéosciences Bordeaux, UMR 6034 CNRS-Université Bordeaux Montaigne, Pessac, France. ²Centro Nacional de Investigación Sobre la Evolución Humana, Burgos, Spain. ³Department of Early Prehistory and Quaternary Ecology, University of Tübingen, Tübingen, Germany. ⁴Max Planck Institute for Evolutionary Anthropology (MPI-EVA), Leipzig, Germany. ⁵Department of Anthropology and Archaeology, University of Bristol, Bristol, UK. ⁶Univ. Bordeaux, CNRS, Ministère de la Culture, PACEA, UMR 5199, Pessac, France. ⁷Univ. Bordeaux, CNRS, Bordeaux INP, CBMN, UMR 5248 and Bordeaux Proteome Platform, Bordeaux, France. ⁸Laboratoire des Sciences du Climat et de l'Environnement (LSCE/IPSL UMR CEA/CNRS/UVSQ – Université Paris Saclay), Gif-sur-Yvette, France. ⁹Centre de Recherche en Archéologie, Archéosciences, Histoire (UMR 6566 CReAAH), Rennes, France. ¹⁰Chaire de Paléanthropologie, CIRB, Collège de France, Université PSL, CNRS, Paris, France. ¹¹Histoire Naturelle de l'Homme Préhistorique, UMR 7194 CNRS-Muséum National d'Histoire Naturelle, Paris, France. ¹²Géosciences Rennes, UMR 6118 CNRS - Université de Rennes, Rennes, France. ✉email: mailys.richard@u-bordeaux-montaigne.fr

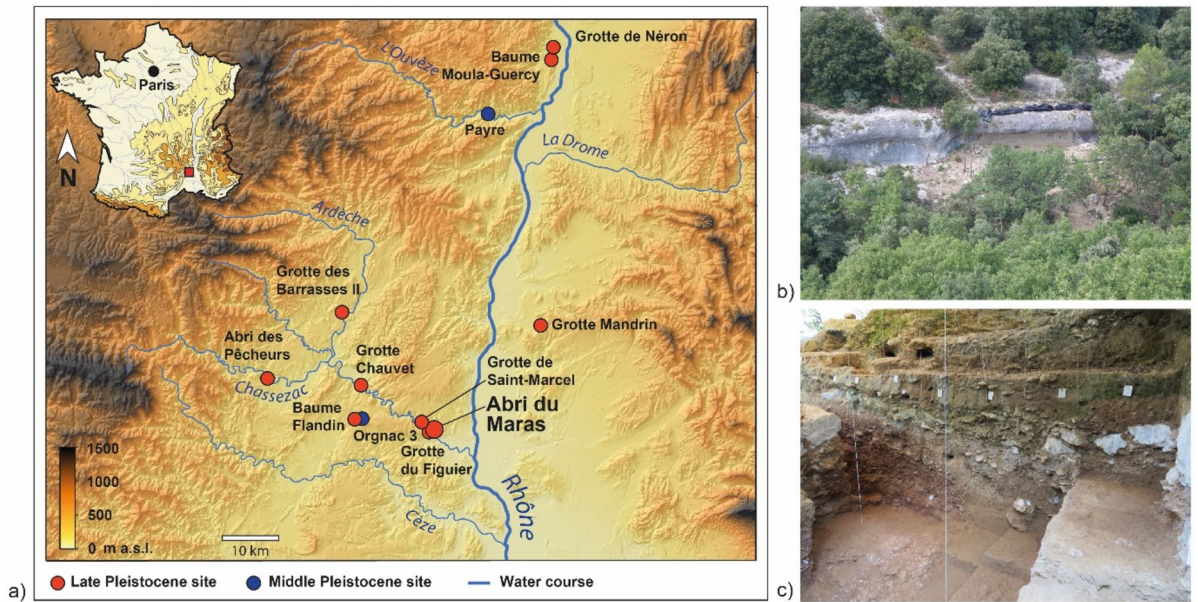


Figure 1. Location of Middle and Late Pleistocene sites in the middle Rhône Valley, France (a, modified from⁵), view of the rock shelter (b) and of the stratigraphy (c).

Thanks to a long-term collaboration in the field between the different specialists working at the site, it has been possible to constrain the chronology as the excavations progressed. Indeed, since the excavations started more than twenty years ago, material for dating has been collected for different methods, including teeth and bones for electron spin resonance (ESR) and uranium-series ($^{230}\text{Th}/\text{U}$) dating, sediment for infrared stimulated luminescence (IRSL) of feldspar and soda straw for U-series^{5,6,10}. More specifically, the Middle Palaeolithic level 4.1 located at the top of the sequence, is dated to ca. 46–40 ka⁶, contemporary with the beginning of the Upper Palaeolithic in Europe (e.g.,^{11–14}). However, the base of the stratigraphic sequence, which shows similarities with the material excavated at Payre, has not been precisely dated. So far, only a maximum age obtained on soda straw, ca. 429 ka, is available for layer 6⁵ (Fig. 2). This study is focused on constraining the chronology of the lower part of the sequence (layers 6 and 5 upper), using optically stimulated luminescence (OSL) on quartz recovered from the sediment, and ESR/U-series dating on tooth enamel. It also aims at increasing the resolution of the timeline for the upper part of the sequence, combining non-destructive near infrared (NIR) spectroscopy for collagen pre-screening with radiocarbon (^{14}C) dating to provide an age for the last occupation period by Neanderthals.

Collagen peptide mass fingerprinting, specifically zooarchaeology by mass spectrometry (ZooMS), has been applied to the fragmentary bone specimens dated through radiocarbon. This complementary method contributes to the accuracy and reliability of contextual documentation in chronological analyses. ZooMS is a minimally destructive proteomic method that focuses on morphologically unidentifiable bone fragments, and can provide a taxonomic identification based on protein amino acid sequence variation through the analysis of collagen protein type I.

These new chronological data are essential to discuss the emergence of the Middle Palaeolithic, and more generally the diachronic variability of Neanderthal behaviour prior to the lasting occupation of the region by *Homo sapiens*, which may have led to their disappearance.

Maras rockshelter Site description

Located in the Ardèche gorge (Fig. 1), the Abri du Maras (44°18'43.4"N 4°33'46.2"E; 170 m asl) is a rock shelter that was first excavated in the 1950s and 1960s by R. Gilles and J. Combier¹⁵. Since the 2000s, excavations have been conducted by M.-H. Moncel.

The new stratigraphy is composed of several layers, numbered from 6 (bottom) to 1 (top) (Fig. 2). A detailed description of the stratigraphy and a map showing the different excavation areas can be found in the Supplementary Material (Fig. S1). Two phases of roof collapse occurred between layers 5 upper and 4, and between layers 3 and 2. Most of the archaeological material was recovered in layers 6, 5 upper-5 and 4. The top of the sequence contains a low density of artefacts, possibly disturbed by a sheep pen used in the 1960s. Correlations of the newly excavated sequence in the eastern part of the site with the stratigraphy of J. Combier and R. Gilles¹⁵ at the western limit of the site are difficult due to differences in depths and thickness between the two areas, due to the erosion of sediments in the western area (Fig. S1 in Supplementary Material). R. Gilles and J. Combier completely excavated layer 1 and no section is now visible.

Limestone bedrock was reached at the front of the present-day shelter and shows a series of steps towards the shelter wall. Cryoclastic elements and coarse deposits were identified at the base of the sequence in layer 6 in a red sediment composed of limestone blocks and red silty-sandy deposits. Small soda straw stalactites indicate a

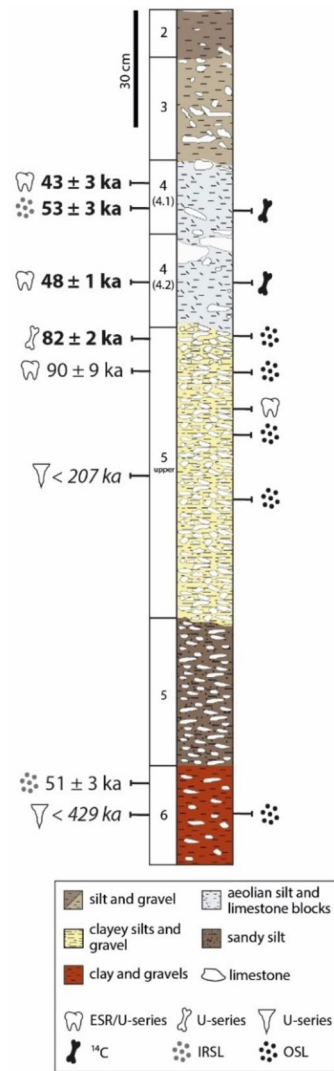


Figure 2. Stratigraphic sequence of Maras rock shelter, with the previous dating results displayed in Table 1 on the left (regular: individual age; bold: weighted mean age; italic: maximum age) and the location of the new samples dated in this study on the right. Note that layer 4 is subdivided into two phases of human occupation (levels 4.1 and 4.2) and that levels 5.1, 5.2 and 5.3 are phases of human occupation of layer 5 upper, present only in the eastern part of the site and thus not represented here.

roof was present in the past that is now totally collapsed. Remains of this deposit cover the limestone substratum, preserving it from erosion.

Layer 5 upper is thick and subdivided into three main occupation phases (5.1, 5.2, 5.3) with a higher density of material at the bottom. It rests on layer 5 s.s., which is a stonier deposit. The thickness of layer 5 upper-5 varies according to their location on the site. The greatest thickness (around 70–80 cm) is in the eastern part of the site, composed of brown silty and stony lenses with various extensions. These brown stony layers with a gentle slope are truncated in the front of the site, 10 m from the present-day shelter, eroded in part by the development of the small valley and covered by large blocks coming from the major collapse of the roof. Occupations during layers 5 upper and 5 occurred prior to the first phase of roof collapse, as indicated by the type of deposits, when the cave was larger than the present-day rock shelter.

A layer of between 50 cm and more than 1 m of limestone blocks (corresponding to the first collapse phase of the shelter) separates layer 5 upper-5 from overlying layer 4, the latter being subdivided into levels 4.1 and 4.2, which are the two main phases of human occupation. Layer 4 is composed of poorly sorted blocks of roof spall embedded in a silt matrix with a sterile loess deposit between the two phases of occupation^{16–20}. These occupations took place beyond the present-day dripline due to the subsequent collapse of the overhang of the shelter. The more recent occupations, documented at the top of the sequence, took place in a shelter configuration, after the second phase of roof collapse between layers 3 and 2. The deposits documenting the final occupations are sparse due to historical disturbance from the animal pen.

Archaeological assemblages

The layer 6 assemblage shows a low density of archaeological material, with artefacts made predominantly of quartz and quartzite, with some flint. Cores and flakes are on flint. Quartz pebbles and large quartzite cobbles produced small quartz flakes and large quartzite flakes. Few retouched flakes have been recovered up to now. The faunal remains are highly fragmented.

In layer 5 upper-5, the core technologies are more diversified, and more retouched flakes were uncovered, mainly made of flint coming from southern outcrops¹⁸. Some evidence of semi-Quina tools is observed in the diversified core technology and evidence of an early Rhodanian Quina facies raises questions. The in-situ core technologies are diversified with discoid, orthogonal, multidirectional and Levallois cores, and cores on flake. The retouches on flakes are more invasive and the ratio of retouched flakes is higher than for the upper phase of occupation. Evidence of *Alnus* root processing is documented in layer 5²¹.

In layer 4, Levallois core technology was used to produce flakes, blades and points, mainly from flint, associated to other types of core technologies, such as discoid-type cores made in situ. Flake-tools are rare, including some imported Quina scrapers made on large and thick flakes. The largest products (points, flakes, blades) were imported unretouched in a tool kit from a 30 km perimeter around the site where flint was collected¹⁶. The site has provided considerable information regarding Neanderthal behaviour and cognitive capacity; fibre technology was evidenced through residue analyses²², in particular the identification of 3-ply cordages in level 4.2²³, dated using ESR/U-series to 55 ± 2 ka to 40 ± 3 ka⁶.

Regarding faunal remains, herbivores dominate the assemblage. Deer (*Cervus* sp.), roe deer (*Capreolus capreolus*) and wild boar (*Sus scrofa*) are present at the base of the sequence, indicating a forest environment. At the top of the sequence, species such as reindeer (*Rangifer tarandus*), bison (*Bison* sp.), and horse (*Equus* cf. *Germanicus*) are the most abundant, and suggest increasingly cold conditions from the bottom to the top of the sequence^{24,25}. In layer 5 upper-5, the corpus is diversified with *Sus scrofa*, *Capreolus capreolus*, *Capra ibex*, *Equus hydruntinus*, *Dama dama* and *Oryctolagus cuniculus*. No carnivore marks were identified and a great number of cut marks were observed, indicating an anthropic origin of the osseous accumulation. Burnt bone, together with charcoal, were also recovered in layers 4 and 5¹⁸. Intensive exploitation of natural resources is consistent with a residential campsite for long-term occupation events during a whole season, mainly summer, for layer 5 upper-5²⁵, while for layer 4, short-term occupations took place mainly in autumn^{18,24,26}.

Previous dating

Several dating methods have been applied since the 2000s (Table 1). U-series analyses were conducted on bones and teeth, but since the time between the burial and the uranium uptake in the tissues is unknown, these only provide minimum age estimates^{27,28}. For this reason, U-series on fossil teeth is generally combined with electron spin resonance (ESR) to model the U-uptake and obtain more precise ages, providing that no U-leaching occurred during burial time²⁹. On the other hand, when applied to soda straws found in sediment, U-series gives a maximum age to the archaeological deposit, considering that these thin stalactites break shortly after precipitation, events that precede their incorporation to the sediment (e.g.,³⁰). Luminescence dating was also applied to date the time of sediment deposition: when applied to feldspar minerals, infrared stimulated luminescence gives the age of the last exposure of the sediment to sunlight (“bleaching”), i.e., during transportation prior to deposition in the site³¹.

Previous dating results allowed framing Neanderthal occupation at the site between MIS 5 and 3 (Table 1). In particular, U-series provided a minimum age for bones from layer 5 upper, ranging from ca. 90 to 70 ka¹⁰. Soda straws from layer 6 and 5 upper gave a maximum age ranging from 429 ± 32 ka (layer 6) to 207 ± 3 ka (layer 5 upper)⁵. ESR/U-series on fossil teeth yielded ages from 90 ± 9 ka (layer 5 upper) to 40 ± 3 ka (layer 4.1). IRSL applied to multi-grain feldspar aliquots provided ages from 51 ± 3 ka (layer 6) to 46 ± 4 ka (level 4.1 in layer 4). These data indicate that human occupation occurred during MIS 5 at the base of the sequence (layer 5 upper) and during MIS 3 at the top of the sequence (levels 4.2 and 4.1), suggesting that MIS 4 is either not recorded at the site or was eroded.

Results

Radiocarbon and palaeoproteomics

Thirty-five bone fragments belonging to large herbivores were non-destructively pre-screened with NIR spectroscopy to assess their collagen preservation prior to destructive sampling, and 11 were selected for collagen extraction. The pretreatment information and radiocarbon ages obtained are presented in Table 2. The collagen yields from the pretreated bones were low (0.8–3.9%), as indicated by the NIR pre-screening, but fall within the range expected for material of this age, with only one below the ~1% minimum requirement for dating³². The elemental values of all extracts fall within accepted ranges of well-preserved collagen (C: ~30–50%; N: 11–15%; C:N: 2.9–3.6)^{33–35} with no indications of contamination.

Two bone collagen extracts from level 4.1 and four from level 4.2 were selected for dating with accelerator mass spectrometry (AMS). The six ¹⁴C dates fall in MIS 3, between 44,840 and 39,280 cal BP (at 95.4% probability) from level 4.2 and 41,480–39,930 cal BP from level 4.1 (Table 2). The dates obtained are in good agreement with the previous ESR/U-series ages on tooth enamel from the same levels (Table 1). The ¹⁴C dates were obtained from anthropogenically modified material, indicating human occupation during this interval, and provide a more precise chronological range for the layer 4 assemblage than the dates previously obtained from ESR/U-series.

Four dates from level 4.2 (ETH-111907, ETH-118371, ETH-118372 and ETH-118373) have a spread of ages that do not overlap at the 95.4% range, whereas the two dates from level 4.1 (ETH-118369 and ETH-118370) are statistically indistinguishable (X^2 test: $T = 1.238$ (5% 3.841), $df = 1$). However, the age of M6-1085 (ETH-118372) in level 4.2 overlaps with the dates from 4.1, indicating it may have moved into 4.2 from the sublayer above.

| Layer/Level | Sample # | Method / Material | Age (ka) | References |
|---------------|--------------|---------------------------------------|----------|---------------------------------|
| 5 upper (l-m) | AM-C5-K4-107 | U-series (alpha spectrometry) / bones | 87 ± 5 | Moncel and Michel ¹⁰ |
| 5 upper (l-m) | AM-C5-L1-116 | | 89 ± 4 | |
| 5 upper (l-m) | AM-C5-L3-134 | | 91 ± 4 | |
| 5 upper (l-m) | AM-C5-M2-155 | | 72 ± 3 | |
| 4/4.1 | AM L6-221 | ESR/U-series / tooth enamel | 46 ± 3 | Richard et al. ⁶ |
| 4/4.1 | AM L6-229 | | 40 ± 3 | |
| 4/4.2 | AM L6-769 | | 42 ± 3 | |
| 4/4.2 | AM G6-203 | | 46 ± 6 | |
| 4/4.2 | AM J6-393 | | 55 ± 2 | |
| 5 upper | AM F6-47 | | 90 ± 9 | |
| 4/4.2 | AM L11-412 | ESR/U-series / tooth enamel | 42 ± 3 | Richard et al. ⁵ |
| 4/4.2 | AM M10-369 | | 42 ± 6 | |
| 4/4.1 | WLL922 | IRSL / feldspar | 46 ± 4 | Richard et al. ⁵ |
| 4/4.1 | WLL923 | | 63 ± 3 | |
| 6 | WLL924 | | 51 ± 3 | |
| 5 upper | AM L10-300 | U-series (MC-ICPMS) / soda straw* | sup 500 | Richard et al. ⁵ |
| 5 upper | AM M6-1199 | | sup 500 | |
| 5 upper | AM L8-153 | | 207 ± 3 | |
| 5 upper | AM L10-307 | | 377 ± 12 | |
| 5 upper | AM M8-524 | | 370 ± 14 | |
| 5 upper | AM M6-1632 | | sup 500 | |
| 5 upper | AM L10-170 | | sup 500 | |
| 5 upper | AM N6-1001 | | 389 ± 17 | |
| 5 upper | AM O9-27 | | sup 500 | |
| 5 upper | AM O9-23 | | 497 ± 48 | |
| 5 upper | AM M10-554 | | 434 ± 23 | |
| 5 upper | AM L8-249 | | sup 500 | |
| 6 | AM U10-503 | | 429 ± 32 | |
| 6 | AM L13-46 | | sup 500 | |
| 6 | AM L14-05 | | sup 500 | |
| 6 | AM L13-45 | | sup 500 | |
| 6 | AM M12-74 | sup 500 | | |

Table 1. Synthesis of chronological data obtained at Maras rock shelter. Note that layers l-m from Moncel and Michel¹⁰ are equivalent to layer 5 upper and that U-series obtained on soda straw represent a *terminus post quem*. Sup 500 = Secular equilibrium has been reached thus precluding age calculation (samples older than 500 ka).

| AM # | Level | Material | % Collagen | $\delta^{13}\text{C}$ (‰) | $\delta^{15}\text{N}$ (‰) | %C | %N | C:N | ETH lab num | C14 BP | Error | 1 σ cal BP (68.3%) | | 2 σ cal BP (95.4%) | |
|---------|-------|----------------|------------|---------------------------|---------------------------|------|------|-----|-------------|--------|-------|---------------------------|--------|---------------------------|--------|
| | | | | | | | | | | | | From | To | From | To |
| I6-223 | 4.1 | Reindeer tibia | 1.1 | -20.0 | 6.0 | 42.5 | 15.1 | 3.3 | | | | | | | |
| L6-289 | 4.1 | Reindeer tibia | 1.0 | -19.4 | 7.0 | 35.7 | 12.6 | 3.3 | ETH-118369 | 35,880 | 280 | 41,220 | 40,740 | 41,480 | 40,450 |
| M6-318 | 4.1 | Reindeer tibia | 1.5 | -20.2 | 5.6 | 37.4 | 13.2 | 3.3 | ETH-118370 | 35,420 | 260 | 40,920 | 40,290 | 41,090 | 39,930 |
| M6-421 | 4.1 | Reindeer tibia | 1.5 | - | - | - | - | - | | | | | | | |
| E7-208 | 4.2 | Reindeer tibia | 2.2 | -19.6 | 3.9 | 40.1 | 14.2 | 3.3 | | | | | | | |
| H6-241 | 4.2 | Bison tibia | 3.9 | -19.7 | 4.8 | 42.5 | 15.2 | 3.3 | ETH-118371 | 41,070 | 510 | 44,530 | 43,410 | 44,840 | 43,080 |
| L6-1001 | 4.2 | Bison tibia | 1.2 | -20.0 | 5.1 | 36.8 | 12.9 | 3.3 | | | | | | | |
| M6-1085 | 4.2 | Bison tibia | 1.0 | -19.6 | 6.6 | 40.5 | 14.2 | 3.3 | ETH-118372 | 34,560 | 240 | 39,970 | 39,430 | 40,360 | 39,280 |
| M7-166 | 4.2 | Cervid tibia | 0.8 | - | - | - | - | - | | | | | | | |
| F6-24 | 4.2 | Reindeer femur | 1.9 | -19.6 | 5.2 | 42.2 | 14.7 | 3.3 | ETH-118373 | 36,440 | 300 | 41,720 | 41,200 | 41,950 | 41,000 |
| M10-542 | 4.2 | Bison | 3.6 | -19.5 | 5.9 | 40.5 | 14.4 | 3.3 | ETH-111907 | 37,990 | 240 | 42,390 | 42,170 | 42,500 | 42,040 |

Table 2. Pretreatment and radiocarbon data from bones from Maras. Note that 35 anthropogenically modified bones were screened for collagen preservation prior to analysis; 11 were selected for collagen extraction and 10 also analysed through ZooMS to determine the taxon (Table 3). Six were chosen for dating.

| ZooMS sample # | Square | Specimen ID | Level | R-EVA number | Sample weight (mg) | ZooMS Barcode ID |
|----------------|--------|-------------|-------|--------------|--------------------|--------------------------|
| AM-281 | I6 | 223 | 4.1 | 3736 | 15 | <i>Rangifer tarandus</i> |
| AM-282 | L6 | 289 | 4.1 | 3737 | 17.8 | <i>Rangifer tarandus</i> |
| AM-283 | M6 | 318 | 4.1 | 3738 | 19.1 | <i>Rangifer tarandus</i> |
| AM-284 | M6 | 421 | 4.1 | 3739 | 12 | <i>Rangifer tarandus</i> |
| AM-285 | E7 | 208 | 4.2 | 3740 | 11.4 | <i>Cervid/Saiga</i> |
| AM-286 | H6 | 241 | 4.2 | 3741 | 14 | <i>Bos/Bison</i> |
| AM-287 | L6 | 1001 | 4.2 | 3742 | 22.6 | <i>Bos/Bison</i> |
| AM-288 | M6 | 1085 | 4.2 | 3743 | 14.1 | <i>Cervid/Saiga</i> |
| AM-289 | M7 | 166 | 4.2 | 3744 | 13.1 | <i>Bos/Bison</i> |
| AM-290 | F6 | 24 | 4.2 | 3746 | 12.5 | <i>Cervid/Saiga</i> |

Table 3. ZooMS taxonomic identification of the bone specimens analysed for radiocarbon dating.

However, there are no other indications of movement (anatomical bones were found in connection, lithic refits are present in the same level, ashes lenses were documented undisturbed).

As the bone fragments had been morphologically identified as belonging to large herbivores, they were analysed with ZooMS to determine the genus/species. ZooMS spectra obtained from ten of the bone specimens selected for collagen extraction were taxonomically identified as *Rangifer tarandus* (reindeer, NISP = 4), *Cervid/Saiga* (NISP = 3) and *Bos/Bison* (NISP = 3) (Table 3). Collagen type I peptide marker series can be similar for some closely related species, which is notably the case for the species belonging to the following taxonomic groups: *Bos/Bison* and *Cervid/Saiga*.

Cervid/Saiga can be attributed to either *Cervus elaphus* (red deer), *Megaloceros giganteus* (giant deer), *Alces alces* (elk), *Dama* sp. (fallow deer) or *Saiga tatarica* (saiga antelope). Taxonomic identifications provided by ZooMS align with those obtained through comparative morphology for six specimens. However, four specimens initially classified as reindeer ($n = 2$), cervid ($n = 1$), or Bison ($n = 1$) have been re-identified as *Cervid/Saiga* ($n = 3$) and *Bos/Bison* ($n = 1$). This underscores the value of applying ZooMS alongside morphological methods for a more comprehensive assessment of the context of these dated specimens.

Trapped-charge dating

OSL ages are presented in Table 4 and Fig. 3 and were obtained following the measurement protocol in Table 8: they range from 247 ± 34 ka for layer 6 at the base to 115 ± 13 ka for the transition between levels 5.1 and 4.2. According to the preheat (PH) plateau test results, a temperature of 220°C was selected for preheating the samples, for which the best recovery ratio of 0.88 ± 0.05 was obtained on AM-06. The dose recovery test (DRT) conducted on AM-01 and AM-06 (nine aliquots each) gave ratio values of 0.85 ± 0.09 and 0.90 ± 0.08 respectively. The equivalent doses obtained are included between 211 ± 8 and 127 ± 4 Gy, with overdispersion (OD) values ranging from 25 to 11% respectively (Table 4). An example of dose response curve is given in Fig. 4. In general, samples are homogeneous, only three samples out of seven have OD values $\geq 21\%$. For this reason, the central age model (CAM³⁶) was used for age calculation. Regarding the environmental dose rate, similar values were obtained within a layer; however, across the sequence, dose rate values range from 767 ± 64 (layer 6) to 2018 ± 97 $\mu\text{Gy}\cdot\text{a}^{-1}$ (layer 5.1). The heterogeneity of the dosimetric environment is due to the nature of the dated layers and particularly to the presence of numerous blocks of limestone that affect the dose rate (Fig. 3).

Considering the 1σ error, the OSL ages follow the stratigraphic order and are in agreement within each layer. A weighted mean age can be calculated for layers 6 and 5 upper, for which two samples were analysed. They are 235 ± 33 ka and 111 ± 16 ka respectively. Level 5.2 is dated to 127 ± 17 ka and 5.1 to 105 ± 13 ka. An age of 115 ± 13 ka was obtained for the transition between levels 5 and 4.2. In general, ages from layer upper 5 (obtained

| Sample # | Layer/Level | Square | n | D _e (Gy) | OD (%) | Dose rate ($\mu\text{Gy}\cdot\text{a}^{-1}$) | | | | Age (ka) |
|----------|-------------|--------|----|---------------------|------------|--|--------------|-------------|---------------|--------------|
| | | | | | | Beta | Gamma | Cosmic | Total | |
| AM-01 | 4.2–5.1 | K5/K6 | 21 | 127 ± 4 | 11 ± 2 | 581 ± 16 | 454 ± 7 | 70 ± 10 | 1105 ± 20 | 115 ± 13 |
| AM-02 | 5u | K8/L8 | 18 | 162 ± 7 | 16 ± 3 | 920 ± 27 | 493 ± 71 | 63 ± 10 | 1476 ± 77 | 110 ± 16 |
| AM-03 | 5u | K9/L9 | 18 | 160 ± 8 | 18 ± 4 | 876 ± 21 | 491 ± 71 | 57 ± 10 | 1424 ± 75 | 112 ± 16 |
| AM-06 | 5.1 | L5/L6 | 45 | 211 ± 8 | 25 ± 3 | 1146 ± 33 | 809 ± 90 | 63 ± 10 | 2018 ± 97 | 105 ± 13 |
| AM-07 | 5.2 | N9/N10 | 46 | 180 ± 6 | 21 ± 2 | 849 ± 21 | 518 ± 72 | 52 ± 10 | 1419 ± 76 | 127 ± 17 |
| AM-04 | 6 | K9/L9 | 18 | 171 ± 12 | 27 ± 5 | 392 ± 10 | 323 ± 61 | 52 ± 10 | 767 ± 64 | 223 ± 33 |
| AM-05 | 6 | K9/L9 | 22 | 199 ± 7 | 15 ± 3 | 440 ± 10 | 314 ± 60 | 52 ± 10 | 806 ± 62 | 247 ± 34 |

Table 4. OSL results (1σ) presented as a function of the stratigraphic order. The equivalent doses (D_e) were calculated using the central age model (CAM³⁶). 5u = 5 upper; n = number of accepted aliquots, OD = overdispersion.

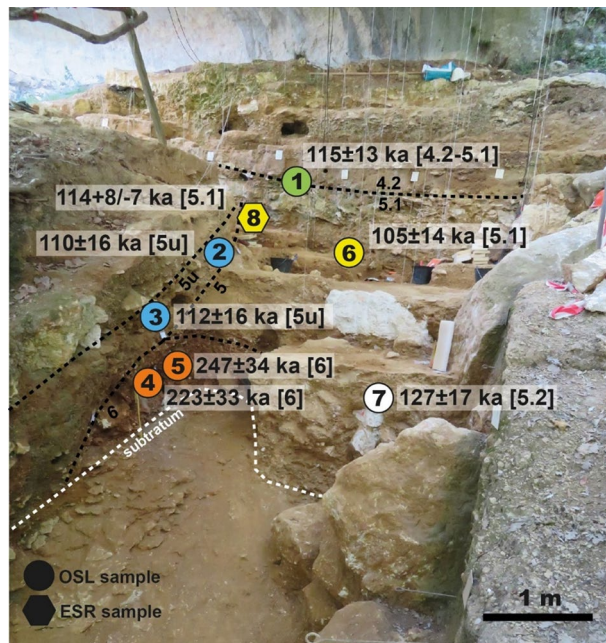


Figure 3. Location and ages (1σ) of the OSL samples (circles) and of the ESR/U-series sample (hexagon) in layers 6 (orange), and 5 upper (blue), and levels 5.2 (white), 5.1 (yellow) and the transition between 5.1 and 4.2 (green).

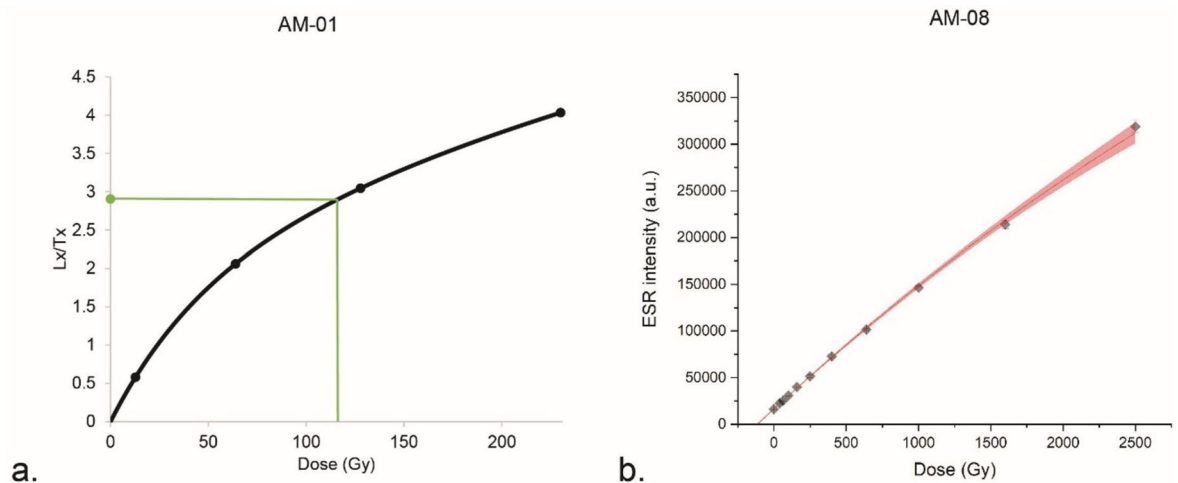


Figure 4. Dose response curves obtained on quartz (a: AM-01) and on hydroxyapatite (b: AM-08), of 124 ± 6 Gy and 115 ± 3 Gy respectively.

on the western part of the site) and level 5.2 and 5.1 on the eastern part (layer 5 upper), and the transition to level 4.2 (eastern part of the site, layer 4) fall in the same range. Indeed, the resolution of the OSL ages (ca. 10%) does not allow differentiating phases of human occupation within MIS 5 for this part of the sequence.

The combined ESR/U-series age (1σ) is given in Table 5 and shown in Fig. 3. The equivalent dose is 115 ± 3 Gy, and the dose response curve is shown in Fig. 4. Due to low U-content in the enamel (Table 6), the main contribution to the dose rate comes from the sediment. Isotopic ratios $^{234}\text{U}/^{238}\text{U}$ and $^{230}\text{Th}/^{234}\text{U}$ gave apparent U-series ages of ca. 28 ka (enamel) and ca. 47 ka (dentine), describing a recent ($p = 1.84 \pm 0.23$) and close to linear uptake ($p = 0.22 \pm 0.12$) respectively. Moreover, the contamination in exogenous Th, assessed through the measurement of $^{230}\text{Th}/^{232}\text{Th}$, is negligible, with ratios $> 147^{37}$. An ESR/U-series age of $114 \pm 8/-7$ ka was obtained for AM-08, in agreement with the OSL age of 105 ± 13 ka obtained for level 5.1 (AM-06), confirming a MIS 5 chronology for this part of the sequence.

| Sample # | Level | Square | D _e (Gy) | Dose rate (μGy/a) | | | | | Age (ka) |
|----------|-------|--------|---------------------|-------------------|-------------|-----------------------|--------------|-----------|------------|
| | | | | Enamel (α + β) | Dentine (β) | Sediment (γ + cosmic) | Sediment (β) | Total | |
| AM-08 | 5.1 | K7 | 115 ± 3 | 36 ± 7 | 115 ± 21 | 774 ± 47 | 87 ± 12 | 1011 ± 53 | 114 + 8/-7 |

Table 5. ESR/U-series dating results (1 σ) for tooth sample AM-08. U-uptake was reconstructed using the ESR-US model²⁹, which takes into account U-content, ²³⁴U/²³⁸U and ²³⁰Th/²³⁴U in the enamel and the dentine (see Table 6).

| Tissue | Labcode | [²³⁸ U] ppm | [²³² Th] ppb | (²³⁴ U/ ²³⁸ U) | (²³⁰ Th/ ²³⁴ U) | (²³⁰ Th/ ²³² Th) | Apparent age (ka) | p-value |
|---------|---------|-------------------------|--------------------------|---------------------------------------|--|---|-------------------|-------------|
| Enamel | 9761 | 0.73 ± 0.01 | 3.59 ± 0.03 | 1.0725 ± 0.0011 | 0.2230 ± 0.0007 | 147.3 ± 0.5 | 27.5 ± 0.1 | 1.84 ± 0.23 |
| Dentine | 9821 | 33.21 ± 0.27 | 4.20 ± 0.03 | 1.0575 ± 0.0011 | 0.3507 ± 0.0008 | 8890.4 ± 18.7 | 47.0 ± 0.2 | 0.22 ± 0.12 |

Table 6. U-series results used for U-uptake modelling and corresponding p-values. Apparent ages are not used in the age calculation but are provided for information, as minimum age estimates for each dental tissue.

Bayesian modelling

ChronoModel version 2.0.18 was used to model 36 dates from layers 6 to 4 (level 4.1) (Tables 1, 2, 4 and 5, and Supplementary information). This set of ¹⁴C, ESR/U-series, OSL, IRSL and U-series dates are grouped into 9 Events (Fig. 5a), which are divided into 8 phases (Fig. 5b).

The Event model is based on the assumption that all the dates it contains are contemporary with the event we aim to date (target date). Each event cannot represent a prolonged duration of time. Differences between dates are explained by experimental errors and calibration errors, as in the case of radiocarbon dating. However, larger discrepancies can occur, the origin of which is usually unknown, making a date appear to be an outlier. The property of the Event model is that it can penalise this outlier without the need to make any additional assumptions, and without the need to eliminate it from the analysis. On the other hand, the temporal constraints imposed by the stratigraphy (arrows on the phase graph in Fig. 5b) also penalise outliers if they are in a stratigraphic inversion position. In the present model, there is only one event per phase, except for the "5 upper" phase, which contains two events. Consequently, the estimates for the beginning and end of each phase will be identical, except for the "5 upper" phase. Figure 6 shows the distribution over time of the a posteriori "begin" and "end" of the eight phases of the model, after the Bayesian model has been calculated.

The numerical results are presented in Table 7 and are expressed in calibrated BP (before 1950). This table provides the chronology of the Maras shelter for the phases concerned. The APM column corresponds to the a posteriori mode: this is the date that corresponds to the maximum of the a posteriori date distribution. The HPD begin—HDP end columns give the "Highest Posterior Density" date interval obtained at the 95% confidence level. The APM dates fix the chronology on the time scale, while the HPD intervals indicate the uncertainties surrounding them at the 95% confidence level.

In the supplementary material, Figs. S2, S3, S4 and S5 give details of the results a posteriori, Event by Event. This makes it easy to identify the outliers and to see how the date distribution of the Event is positioned in relation to the dates that make it up: distributions with a grey line for the individual calibrated dates and distributions calibrated by the global model (in colour). When there is only one date in the Event, there may still be an offset: this is due to the action of the stratigraphic constraints of the global model.

Discussion

Since 2000, a total of 36 ages have been obtained at the Maras rock shelter, following a multi-method and multi-material approach (see Tables 1, 2, 5, 6 and Fig. 7). In general, the age results are in good agreement, considering that the data obtained on the soda straws represent a maximum estimate. Two out of three IRSL age results do not follow the stratigraphic order, 63 ± 3 ka (WLL 923, layer 4.1) and 51 ± 3 ka (WLL 924, layer 6). At the time of the sampling, no in-situ dosimetry could be conducted, and considering the high heterogeneity of the deposits due to the presence of limestone blocks, the calculated environmental dose rate, based on a sediment sample (ca. 100 g), may be inaccurate (see discussion in⁵).

The new ESR/U-series age of 114 + 8/-7 ka obtained on level 5.1 (top layer 5 upper) is in agreement with OSL ages of 115 ± 13 ka (AM-01, at the transition between levels 4.2 and 5.1) and 105 ± 13 ka (AM-06, level 5.1) that indicate an MIS 5 chronology for this layer. These ages are slightly older than those obtained using U-series on bones (Fig. 7), but these are generally considered as minimum age estimates (since the time span between the burial and the uranium uptake is unknown, see³⁸ and discussion in⁵).

The first OSL ages obtained at the site allow extending the chronology of the site to ca. 250 ka (layer 6 dated from 247 ± 34 to 223 ± 33 ka), suggesting that the base of the sequence at Maras is coeval with human occupation in Payre^{4,5} located north of the area along the Rhône Valley and attributed to the early Middle Palaeolithic. For layer 5 upper, two ages of 110 ± 16 ka (AM-02) and 112 ± 16 ka (AM-03) were obtained for the western part of the site, in agreement with the ESR/U-series age of 90 ± 9 ka obtained on a tooth from the same layer⁶ (Table 1); the ages of 105 ± 13 ka (AM-06, level 5.1) and of 127 ± 17 ka (AM-07, level 5.2) obtained for the eastern part of the site suggest an MIS 5 chronology. Due to the resolution of the ages obtained using trapped-charge dating methods,

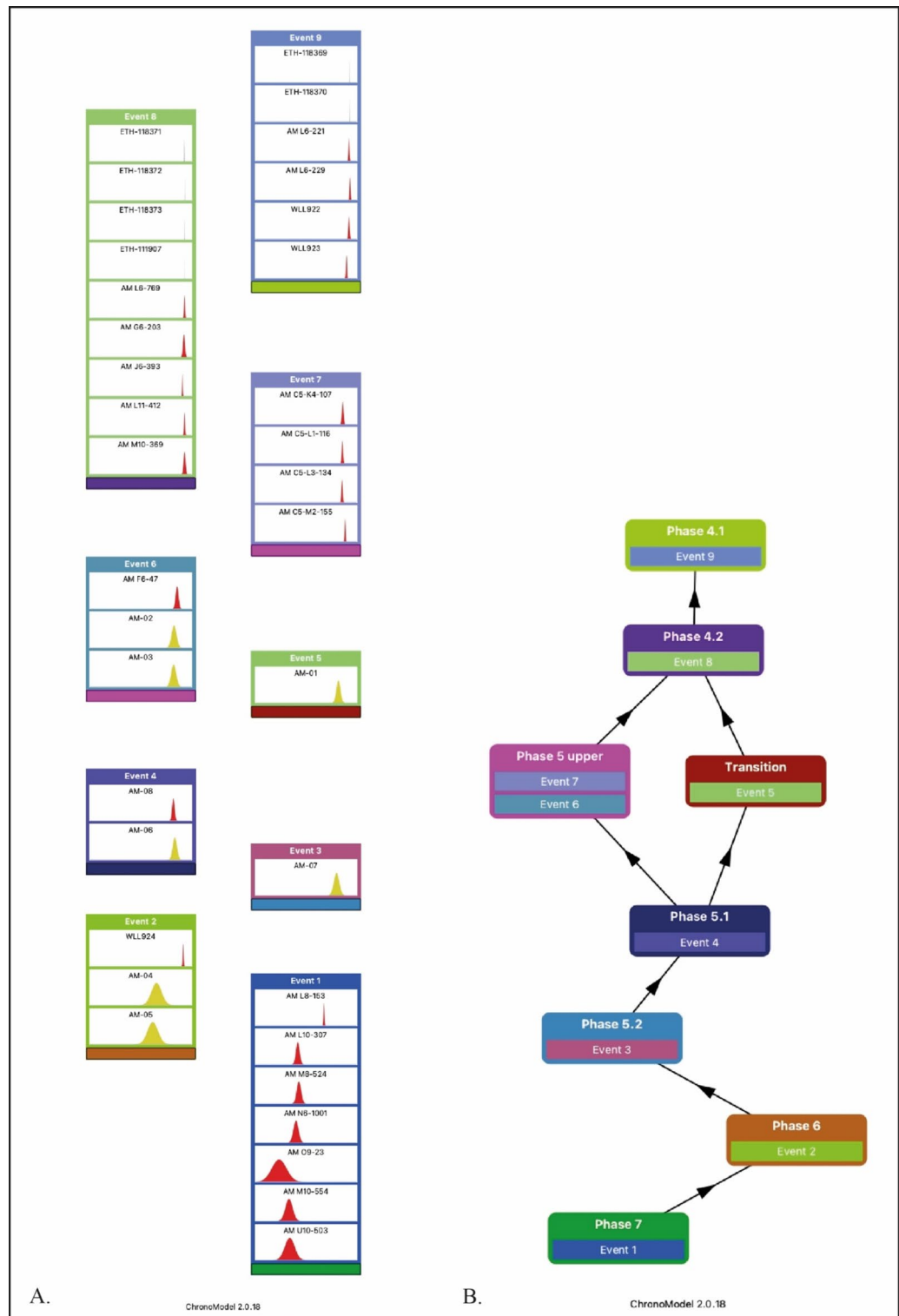


Figure 5. (A) Events model: the 9 Events each contain between 1 and 9 dates which are assumed to be contemporaneous within each Event; (B) Phases model: the 8 Phases contain 1–2 Events. Stratigraphic relationships are represented by arrows going from the oldest to the most recent phase.

we are not able to chronologically distinguish these three phases. However, considering all available data for the site, there is no evidence of MIS 4 deposits, which may be due to erosion processes. A similar chronology is obtained for the nearby sites of the Saint-Marcel cave (level u³⁹) and the Baume Flandin (level 3⁵), dated to MIS 5e.

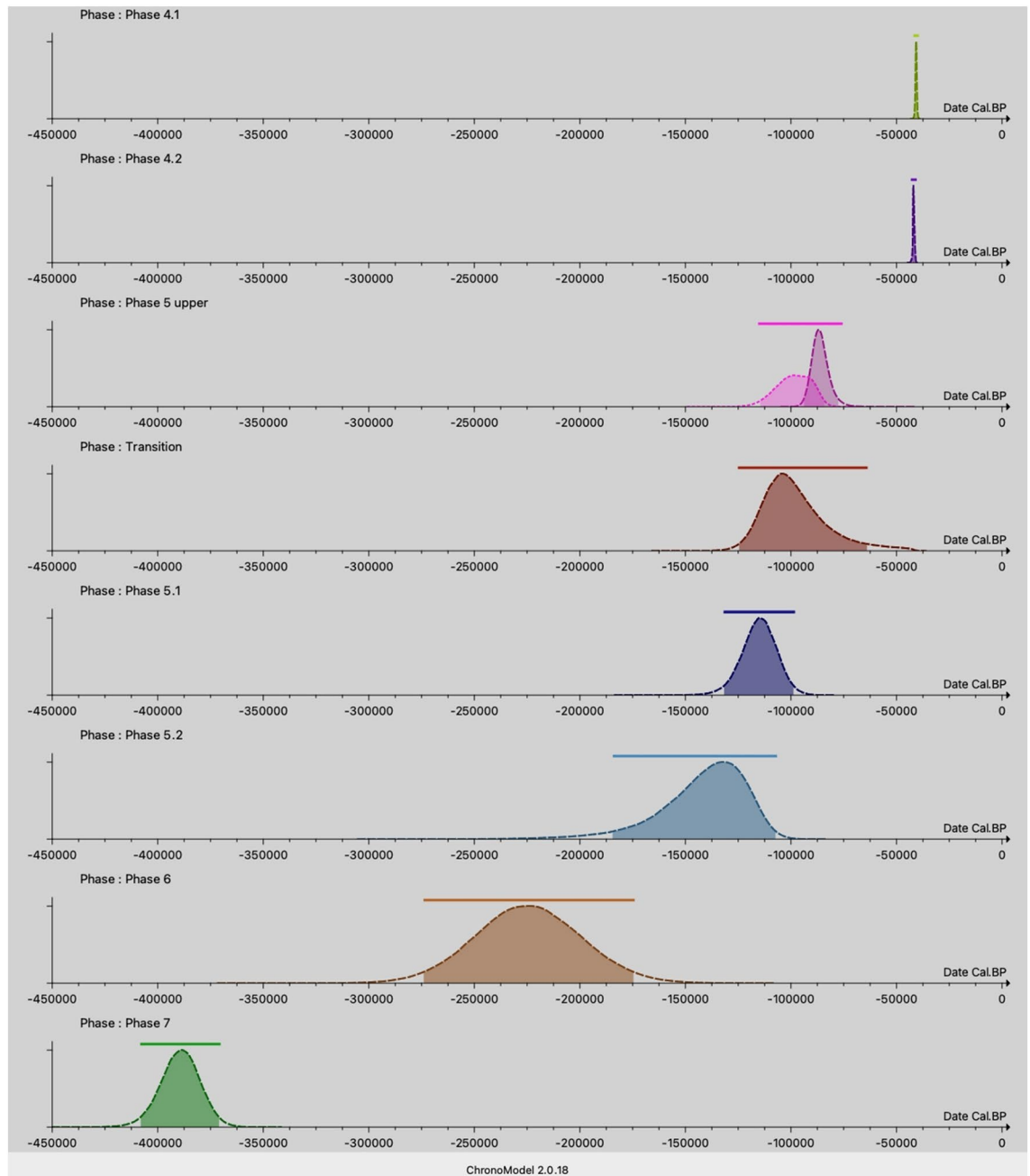


Figure 6. Chronological phasing of the Maras rock shelter: a posteriori date distribution of the beginning and end of each of the 8 phases characterised. The time scale used is cal. BP (before 1950). For phases with only one Event, the start and end distributions are identical. Only phase “5 upper” has two different start and end distributions because it contains two events.

The radiocarbon ages obtained for the top of the sequence confirm that Maras rock shelter was occupied by the latest Neanderthals populations, up to ca. 40 ka BP. Late Neanderthal occupations have also been recorded at the nearby cave of Saint-Marcel (ca. 38 ka BP⁴⁰). These ages coincide with the beginning of the Upper Palaeolithic in Europe attributed to *Homo sapiens*, with directly dated *Homo sapiens* recently shown to be present in Germany as early as 47.5 ka BP¹⁴, suggesting that both groups could potentially have overlapped in this area.

According to the Bayesian model (Fig. 6 and Table 7), and considering the Highest Posterior Density (HPD) date intervals obtained at 95% confidence level, Event 1 (phase 7), dated from the soda straws found in layers 5 upper and 6³, corresponds to an early phase when the roof was still present (cave configuration) between ca. 408 and 371 ka, probably before human visited the cave. Event 2 (layer 6), records the earliest human presence at the site, between ca. 274 (MIS 8) and 175 ka (MIS 6). We need to consider that the Ardèche River and the landscape were completely different at the time of the earliest human occupation; more specifically, during these two phases, the site was possibly a big cave covering the whole end of a small valley, dark and humid (hence the

| Item | Phase | APM | HPD begin | HPD end |
|---------------|------------------|----------|-----------|----------|
| Event 9 | Phase 4.1 | -40,879 | -41,616 | -40,154 |
| Event 8 | Phase 4.2 | -42,191 | -42,790 | -41,167 |
| Event 7 | Phase 5 upper | -87,317 | -94,250 | -79,147 |
| Event 6 | Phase 5 upper | -98,635 | -116,300 | -79,736 |
| Event 5 | Phase Transition | -104,162 | -124,553 | -64,557 |
| Event 4 | Phase 5.1 | -114,367 | -131,739 | -99,092 |
| Event 3 | Phase 5.2 | -132,415 | -184,192 | -107,337 |
| Event 2 | Phase 6 | -226,011 | -273,989 | -174,589 |
| Event 1 | Phase 7 | -388,227 | -408,098 | -371,116 |
| Phase 5 upper | Start | -98,388 | -114,626 | -84,276 |
| Phase 5 upper | End | -87,200 | -94,010 | -77,689 |

Table 7. Summary table of a posteriori statistical results obtained after Bayesian chronological modelling with ChronoModel 3. Dates are expressed in cal BP. APM column: a posteriori mode determined on the a posteriori date distribution. HPD begin—HDP end columns: "Highest Posterior Density" date interval obtained at the 95% confidence level. Note that since Phase 5 upper contains two events (6 and 7), the beginning and the end of the phase can be estimated using Chronomodel. The other phases contain only one event, the beginning and the end of each phase corresponds to the event itself.

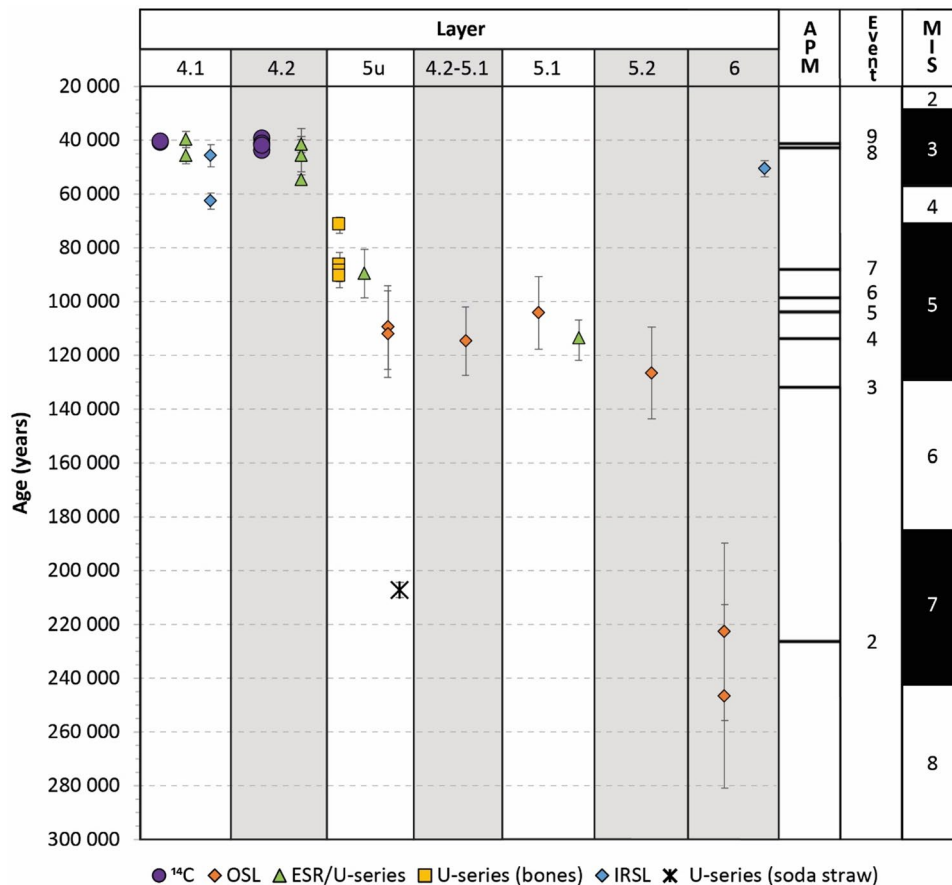


Figure 7. Synthesis of the dating results (1σ) obtained at Abri du Maras. APM (a posteriori mode) for each event are represented, as well as corresponding MIS (marine isotopic stage). Note that due to the scale, the error bars of the radiocarbon dates are not visible, and only the youngest U-series date obtained for layer 5 upper can be represented and thus the APM (388 227 years) as well as the corresponding event (1) are not visible on the figure.

presence of the stalagmites and the red sediments). Blocks were found in the red deposits of layer 6, suggesting that the collapse of the roof started when humans first visited the site. Event 3 (level 5.2) indicates that humans likely occupied the rock shelter between 184 ka (MIS 6) and 107 ka (MIS 5) and Event 4 suggests that level 5.1 would be coeval with MIS 5 (ca. 132–99 ka). A hiatus is observed between the levels 5.1–4.2 transition (Event 5, ca. 125–65 ka, documented in the eastern section of the site, see Fig. 3) and layer 5 upper (Events 6 and 7, ca. 116–79 ka, documented in the western section), and levels 4.2 (Event 8, HPD 42.8–41.2 ka) and 4.1 (Event 9, HPD 41.6–40.2 ka), which fall within MIS 3. The APM, which represents the maximum of the a posteriori date distribution, is 226 ka for layer 6, 132 ka for level 5.2, 114 ka for level 5.1, 104 ka for the transition between levels 5.1 and 4.2, 99 ka for layer 5 upper, 42.2 ka for level 4.2 and 40.9 ka for level 4.1. All these dates fall within interglacial periods, with the exception of the level 5.2, at the transition between MIS 6 and 5. It is thus possible that sediment from glacial periods may not have been preserved or deposited in the site, either due to its location and configuration, or to the climatic conditions.

In conclusion, our new chronological data obtained at Abri du Maras suggest that Neanderthals were present mainly during three interglacial periods: MIS 7, 5 and 3, as indicated by the fauna. During the MIS 3, they hunted mainly *Rangifer tarandus* with rare secondary species (Bovids and Cervids)⁴¹. During the MIS 5, human groups hunted a diversified game including both *Rangifer tarandus* and forested species (*Sus scrofa*, *Dama dama*)⁴² and during the MIS 7, *Cervus elaphus* is the main hunted species (unpublished data). This detailed chronology provides new insights into the timing of the evolution of Neanderthal behaviour at the Maras rock shelter, used as a long-term residence by Neanderthals. Considering that the earliest human presence at the site is dated to ca. 226 ka (APM for layer 6), the human populations from Maras and those from Payre would have been contemporaneous. The site was repeatedly occupied during MIS 5 (layer 5 upper) and 3 (potentially until 39,280 years cal BP). In particular, the ¹⁴C ages allow us to precisely date the last occupation period by Neanderthals between ~41.5 and 39.9 ka, suggesting that these populations would have been among the very last Neanderthal groups settled in the Middle Rhône valley.

Methods

Based on the previous dating results obtained (Table 1), in particular for the upper part of the sequence that falls within the range of radiocarbon dating, bones from levels 4.1 and 4.2 were selected for ¹⁴C dating. During the 2021 excavation campaign, one tooth from level 5.1 was collected for ESR/U-series dating, and sediment from layer 5 upper (western part of the site), levels 4.2–5.1 (transition), levels 5.1 and 5.2 (eastern part of the site) and layer 6 were sampled for OSL of quartz grains (Fig. 2).

Radiocarbon dating

Sample selection and pre-screening

Pre-screening and collagen extraction was carried out in the Department of Human Evolution at the Max Planck Institute for Evolutionary Anthropology (Leipzig, Germany). A selection of 35 long bones (tibia and femur) from large herbivores were pre-screened for collagen preservation to identify suitably preserved material for ¹⁴C dating. Bones were selected from different squares from layer 4 (level 4.1 and 4.2), all bearing signs of anthropogenic modifications. Non-destructive collagen pre-screening was carried out using a LabSpec 4 hi-res near-infrared (NIR) spectrometer (Malvern Panalytical, Germany), following protocols outlined by⁴³. NIR screening indicated low levels of collagen preservation (<5%), as expected for Pleistocene material. Eleven bones were selected for collagen extraction based on their predicted levels (>3%).

Collagen extraction

The surface of the sampled bone was first cleaned with a shot-blaster and between 380 and 590 mg bone was sampled using a dentistry drill with circular drill bit. Collagen was extracted using the protocol described in⁴⁴. Samples were first demineralised in HCl 0.5 M at 4 °C until soft and CO₂ effervescence stopped, with HCl changed once per week. The demineralised samples were treated with NaOH 0.1 M to remove humic acid contaminants and re-acidified in HCl 0.5 M. The samples were gelatinised in HCl pH3 at 75 °C for 20 h. The gelatin extracts were filtered to remove > 80 µm particles (Ezee filters, Elkay Labs, UK) and ultrafiltered to concentrate the > 30 kDa fraction (Sartorius VivaSpin Turbo 15). Filters were pre-cleaned following⁴⁵. After freeze-drying for 48 h, samples were weighed to determine the % collagen yield (as a proportion of dry bone weight) with a minimum ~1% yield requirement.

To assess the quality of each collagen extract prior to dating, ~0.5 mg collagen was weighed into a tin cup using a microbalance and analysed on a ThermoFinnigan Flash elemental analyser coupled to a Thermo Delta plus XP isotope ratio mass spectrometer (EA-IRMS). Stable carbon isotope ratios were expressed relative to VPDB (Vienna PeeDee Belemnite), and stable nitrogen isotope ratios were measured relative to AIR (atmospheric N₂), using the delta notation (δ) in parts per thousand (‰). Analysis of internal and international standards indicates an analytical error of better than 0.2‰ (1σ). All extracts had elemental values (C%, N%, C:N) falling within the range of modern extracts^{32,34,35}, indicating their suitability for dating.

AMS dating and ¹⁴C modelling

Six collagen extracts were selected for dating. The extracts were graphitised⁴⁶ and dated at the Laboratory for Ion Beam Physics at ETH Zurich, Switzerland using a MICADAS accelerator mass spectrometer (AMS)^{47,48}. Aliquots of a background bone (> 50,000 BP) were pretreated and dated alongside the samples to monitor lab-based contamination. The AMS measurements of the collagen backgrounds were used in the age correction of the samples, with an additional 1‰ error added as per standard practise. AMS data reduction was performed in BATS⁴⁹. The ¹⁴C dates were calibrated in OxCal 4.4⁵⁰ using the IntCal20 calibration curve⁵¹.

| Step | Treatment |
|--------|--|
| 1 | Given dose |
| 2 | Preheat (220 °C for 10 s) |
| 3 (Lx) | Blue stimulation for 40 s at 125 °C |
| 4 | Given test dose |
| 5 | Preheat (200 °C for 10 s) |
| 6 (Tx) | Blue stimulation for 40 s at 125 °C |
| 7 | Optical draining (blue stimulation for 40 s at 280 °C) |
| 8 | Return to 1 |

Table 8. OSL SAR measurement protocol applied to quartz.

ZooMS

Ten bone specimens from layer 4 (levels 4.1 and 4.2) selected for collagen extraction for radiocarbon dating were also analysed through Zooarchaeology by mass spectrometry (ZooMS) and sampled destructively (between 11.4 and 22.6 mg) to determine the taxon. Samples analysed through ZooMS followed extraction protocols detailed elsewhere^{52–54}. Each bone sample was demineralised in 250 µl 0.6 M hydrochloric acid (HCl) at 4 °C for 20 h. Samples were then centrifuged for 1 min at 10 k rpm and the supernatant was removed. The demineralized collagen was rinsed three times in 200 µl of ammonium bicarbonate (50 mM, NH₄HCO₃, hereafter AmBic) to be neutralized to pH 8, and 100 µl of AmBic solution was added to each sample. Next, samples were incubated at 65 °C for 1 h. Then, 50 µl of the resulting supernatant was digested with 1 µl of trypsin (0.5 µg/µl, Promega) at 37 °C overnight, acidified using 1 µl of trifluoroacetic acid (20% TFA), and cleaned on C18 ZipTips (Thermo Scientific). Digested peptides were spotted in triplicate on a MALDI Bruker plate with the addition of α -cyano-4-hydroxycinnamic acid (CHCA, Sigma) matrix. MALDI-TOF-MS analysis was conducted at the University of Cambridge, using an UltraFlextreme MALDI-TOF (Bruker) in reflector mode, with matrix suppression up to 500 Da and collected in the mass-to-charge range 700–3500 m/z.

Triplicates of each sample were merged in R v.4.0.5⁵⁵ and MALDIquant v. 1.21⁵⁶. The intensity was smoothed using a moving average and the baseline was removed using the TopHat approach. Then, the replicate spectra were aligned for each sample using SuperSmoother and a signal to noise ratio of 3, and the three replicates were summed to obtain a single spectrum, in addition to another removal of the baseline again using TopHat. Spectra were then exported as .msd files. Taxonomic identifications were made using mMass⁵⁷ through manual peptide marker mass identification in comparison to a database of peptide marker series for all European Pleistocene medium- to large-sized mammals⁵². To assess any potential contamination by non-endogenous peptides, we performed laboratory blanks alongside the samples. These remained empty of collagenous peptides, excluding the possibility of modern laboratory or storage contamination.

Optically stimulated luminescence (OSL)

OSL was applied on sediment collected at night from the fresh sections ($n=7$), and kept in light-proof bags (Fig. 3). A 30-cm deep hole was dug at the location of the samples to conduct in-situ gamma dosimetry, using a portable gamma-ray spectrometer multichannel analyser connected to a NaI(Tl) detector (Inspector 1000, Canberra). The gamma dose rate was obtained for each sample following the “threshold” technique⁵⁸. The excavated sediment was kept to derive the beta dose rate from U, Th and K content measured using mass spectrometry. A water content (water/dry mass of sediment %) of $15 \pm 5\%$ was used for calculation based on the previous dating conducted at the site^{5,6} and used for age calculation. The equivalent doses were obtained following the measurement protocol in Table 8. The data were processed using Analyst v.4.57⁵⁹. The signal was integrated using the first 0.5 s and background was subtracted from the last 2.5 s. The following criteria were applied for D_c selection: a recycling ratio limit of 1 ± 0.1 ; recuperation $< 5\%$ of the natural signal; maximum test dose error of 10%; and a test dose signal > 3 sigma above background. Infrared (IR) depletion assessments were conducted as well⁶⁰. Equivalent doses were obtained using a sum of two exponentials fitting function. OSL ages were calculated with the 1σ error range, taking into account the published alpha attenuation⁶¹ and beta absorption⁶² factors, and the updated dose-rate conversion factors⁶³. The cosmic dose rate was calculated from the equations of Prescott and Hutton⁶⁴. U-series equilibrium was assumed for dose rate calculation.

The samples were sieved and the 150–250 µm fraction was chemically treated to eliminate organic matter (using H₂O₂) and carbonates (using HCl). Density separation (of 2.62 and 2.70) was done to extract the quartz fraction used for analysis. Single aliquot regeneration (SAR⁶⁵) analyses were conducted on multigrain 2 mm aliquots following the protocol displayed in Table 7. A preheat (PH) plateau test was performed on aliquots of AM06, previously bleached in a solar simulator (Hönle UVACube 400 solar simulator) for 2 h. Measurements were conducted with PH temperature between 200 and 260 °C with 20 °C steps, and a given dose of ca. 120 Gy. Dose recovery tests were conducted on bleached aliquots AM-01 and AM-06, with a given dose of ca. 75 Gy.

Combined electron spin resonance/uranium-series dating (ESR/U-series)

The tooth AM-08 (square K7, #598) and the embedded sediment were collected during the excavation campaign in 2021. The dental tissues were mechanically separated and cleaned using a dentist drill in order to conduct ESR analysis on the enamel and U-series analyses on bulk enamel and dentine, following the protocol described

in⁶. The enamel powder (100–200 µm) was split into eleven aliquots, from which ten were irradiated at increasing doses (40, 64, 100, 160, 250, 400, 640, 1000, 1600 and 2500 Gy) using a ¹³⁷Cs gamma source (Gammacell, CENIEH, Burgos, Spain), and one kept intact to measure the natural ESR intensity. The ESR intensity of the carbonate hydroxyapatite T1-B2 signal⁶⁶ of each aliquot was measured three times using an X-band spectrometer (Bruker EMXmicro-6/1) at the CENIEH, with the following parameters: 10–50 scans, 1 mW microwave power, 1024 points resolution, 10 mT sweep width, 100 kHz modulation frequency, 0.1 mT modulation amplitude, 20.48 ms conversion time, and 5.12 ms time constant. The mean value and associated standard deviation were plotted as a function of the irradiation dose. The dose response curve was constructed using Origin Pro 8 (Origin Lab Corporation, Northampton, USA). The equivalent dose was obtained by extrapolation using a single saturation exponential (SSE) function⁶⁷ and weighted by the inverse of the squared ESR intensity ($1/I^2$).

U-series analyses (U and Th content and isotopic ratios ²³⁴U/²³⁸U, ²³⁰Th/²³⁴U and ²³⁰Th/²³²Th) were conducted to model the U-uptake using the ESR-US model, for which an uptake parameter is calculated, the p-value²⁹. Ranging from -1 (describing an early uptake, i.e., U incorporated soon after burial) to positive values (describing a recent uptake), this model allows deriving the dose rate individually for each dental tissue. The chemical analyses were performed at the Laboratory for Science of Climate and Environment (LSCE, Gif-sur-Yvette, France) following the procedure for separation and purification of U and Th isotopes of⁸. U and Th fractions were combined for the measurement on a Multi-Collector inductively coupled plasma mass spectrometer (MC-ICP-MS) Thermo Scientific TM Neptune Plus fitted with a jet pump interface and a desolvating introduction system (aridus II) following⁶⁸. ²³⁸U, ²³⁵U, ²³⁶U and ²²⁹Th were measured on Faraday cups, ²³⁴U and ²³⁰Th on an ion counter (see details in⁶⁹).

U, Th and K content from the sediment containing the tooth was determined using ICP-MS to derive the beta and gamma dose rate. A value of $15 \pm 5\%$ was used for calculation based on the previous ESR dating conducted at the site^{5,6}. For the dental tissues, a water content (weight %) of 0% for the enamel and of $7 \pm 5\%$ for the dentine was assumed. The cosmic dose rate was calculated considering sediment and limestone cover above each sample following Prescott and Hutton⁶⁴. Combined ESR/U-series calculation were performed using the DATA program⁷⁰, which takes into account an alpha efficiency of 0.13 ± 0.02 ⁷¹ and Monte-Carlo beta attenuation factors⁷². U-series equilibrium was assumed for dose rate calculation (dental tissues and sediment).

Bayesian modelling

The ChronoModel Application is intended to provide tools for constructing chronologies in archaeology and geosciences in combining Events, Phases and temporal constraints. Models can be developed including data from any dating methods (¹⁴C, TL/OSL, AM, typo-chronology, etc.) and from archaeological and environmental contexts (stratigraphy, ordering between phases, duration or hiatus constraints)^{73,74}. A user-friendly interface is available for entering the data and MCMC (Markov Chain Monte Carlo) calculations can be carried out and inspected in detail, with models and results presented using the Bayesian statistical framework. ChronoModel is a free and open-source cross-platform software (Mac, Windows, Linux)⁷⁵. It is available for downloading at: <https://chronomodel.com/>. The source code can be downloaded and compiled; the project is hosted on GitHub.com. The repository can be cloned by typing: <https://github.com/Chronomodel/chronomodel.git>. In the present study, the MCMC calculation was carried out with 3 chains of 1 million iterations each, which ensures the convergence of the calculations, i.e., a good estimate of the a posteriori date distributions (probability density), given the data available.

Data availability

The datasets generated during and/or analysed during the current study are available from the corresponding author on reasonable request.

Received: 13 May 2024; Accepted: 5 August 2024

Published online: 03 September 2024

References

1. Michel, V. *et al.* Application of U/Th and ⁴⁰Ar/³⁹Ar dating to Orgnac 3, a late acheulean and early middle palaeolithic site in Ardèche, France. *PLoS One* **8**, e82394. <https://doi.org/10.1371/journal.pone.0082394> (2013).
2. Bahain, J.-J. *et al.* Reappraisal of the chronology of Orgnac 3 lower-to-middle paleolithic site (Ardèche, France), a regional key sequence for the Middle Pleistocene of southern France. *J. Hum. Evol.* **162**, 103092. <https://doi.org/10.1016/j.jhevol.2021.103092> (2022).
3. Masouadi, H. *Application des méthodes du déséquilibre des familles de l'uranium (²³⁰Th/²³⁴U) et de la résonance de spin électronique (ESR) à la datation des sites d'Orgnac 3, de Payre et de l'abri des Pêcheurs (Ardèche)* PhD thesis thesis, Paris, Muséum national d'histoire naturelle (1995).
4. Valladas, H. *et al.* Radiometric dates for the middle palaeolithic sequence of Payre (Ardèche, France). *Quat. Geochronol.* **3**, 377–389. <https://doi.org/10.1016/j.quageo.2008.01.001> (2008).
5. Richard, M. *et al.* Timing of Neanderthal occupations in the southeastern margins of the Massif Central (France): A multi-method approach. *Quatern. Sci. Rev.* **273**, 107241. <https://doi.org/10.1016/j.quascirev.2021.107241> (2021).
6. Richard, M. *et al.* Contribution of ESR/U-series dating to the chronology of late Middle Palaeolithic sites in the middle Rhône valley, southeastern France. *Quat. Geochronol.* **30**, 529–534. <https://doi.org/10.1016/j.quageo.2015.06.002> (2015).
7. Slimak, L. *et al.* Modern human incursion into Neanderthal territories 54,000 years ago at Mandrin, France. *Sci. Adv.* **8**, eabj9496. <https://doi.org/10.1126/sciadv.abj9496> (2022).
8. Quiles, A. *et al.* A high-precision chronological model for the decorated Upper Paleolithic cave of Chauvet-Pont d'Arc, Ardèche, France. *Proc. Natl. Acad. Sci.* **113**, 4670–4675. <https://doi.org/10.1073/pnas.1523158113> (2016).
9. Valladas, H. *et al.* Palaeolithic paintings: Evolution of prehistoric cave art. *Nature* **413**, 479–479 (2001).
10. Moncel, M.-H. & Michel, V. Première datation radiométrique par U-Th d'un niveau moustérien de l'Abri du Maras (Ardèche, France). *Bulletin de la Société préhistorique française*, 371–375 (2000).

11. Higham, T. *et al.* Testing models for the beginnings of the Aurignacian and the advent of figurative art and music: the radiocarbon chronology of Geißenklösterle. *J. Hum. Evol.* **62**, 664–676. <https://doi.org/10.1016/j.jhevol.2012.03.003> (2012).
12. Fewlass, H. *et al.* A ¹⁴C chronology for the Middle to Upper Palaeolithic transition at Bacho Kiro Cave, Bulgaria. *Nat. Ecol. Evol.* **4**, 794–801. <https://doi.org/10.1038/s41559-020-1136-3> (2020).
13. Cortés-Sánchez, M. *et al.* An early Aurignacian arrival in southwestern Europe. *Nat. Ecol. Evol.* **3**, 207–212. <https://doi.org/10.1038/s41559-018-0753-6> (2019).
14. Mylopotamitaki, D. *et al.* *Homo sapiens* reached the higher latitudes of Europe by 45,000 years ago. *Nature* **626**, 341–346. <https://doi.org/10.1038/s41586-023-06923-7> (2024).
15. Comber, J. *Le Paléolithique de l'Ardèche dans son cadre paléoclimatique*. Publication de l'Institut de Préhistoire de l'Université de Bordeaux, 4, edn. (Delmas, 1967).
16. Moncel, M. H. *et al.* Fragmented reduction processes: Middle Palaeolithic technical behaviour in the Abri du Maras shelter, southeastern France. *Quat. Int.* **350**, 180–204. <https://doi.org/10.1016/j.quaint.2014.05.013> (2014).
17. Moncel, M.-H. *et al.* Evaluating the integrity of palaeoenvironmental and archaeological records in MIS 5 to 3 karst sequences from southeastern France. *Quat. Int.* **378**, 22–39. <https://doi.org/10.1016/j.quaint.2013.12.009> (2015).
18. Moncel, M.-H. *et al.* Late Neanderthals short-term and specialized occupations at the Abri du Maras (South-East France, level 4.1, MIS 3). *Anthropol. Archaeol. Sci.* **13**, 45 (2021).
19. Debard, E. *Le Quaternaire du Bas-Vivarais: dynamique sédimentaire, paléoclimatologie et chronologie d'après l'étude sédimentologique des remplissages d'ovens, de porches de grottes et d'abris sous roche: comparaisons avec le Velay oriental* PhD thesis thesis, Université Claude Bernard, Lyon 1, (1988).
20. Puaud, S., Nowak, M., Pont, S. & Moncel, M.-H. Minéraux volcaniques et alpins à l'abri du Maras (Ardèche, France): témoins de vents catabatiques dans la vallée du Rhône au Pléistocène supérieur. *Comptes Rendus Palevol* **14**, 331–341. <https://doi.org/10.1016/j.crpv.2015.02.007> (2015).
21. Miras, Y. *et al.* Neanderthal plant use and stone tool function investigated through non-pollen palynomorphs analyses and pollen washes in the Abri du Maras, South-East France. *J. Archaeol. Sci. Rep.* **33**, 102569. <https://doi.org/10.1016/j.jasrep.2020.102569> (2020).
22. Hardy, B. L. *et al.* Impossible Neanderthals? Making string, throwing projectiles and catching small game during Marine Isotope Stage 4 (Abri du Maras, France). *Quat. Sci. Rev.* **82**, 23–40. <https://doi.org/10.1016/j.quascirev.2013.09.028> (2013).
23. Hardy, B. L. *et al.* Direct evidence of Neanderthal fibre technology and its cognitive and behavioral implications. *Sci. Rep.* **10**, 4889. <https://doi.org/10.1038/s41598-020-61839-w> (2020).
24. Daujeard, C. *et al.* Neanderthal selective hunting of reindeer? The case study of Abri du Maras (south-eastern France). *Archaeol. Anthropol. Sci.* **11**, 985–1011. <https://doi.org/10.1007/s12520-017-0580-8> (2019).
25. Marin, J. *et al.* Neanderthal faunal exploitation and settlement dynamics at the Abri du Maras, level 5 (south-eastern France). *Quat. Sci. Rev.* **243**, 106472. <https://doi.org/10.1016/j.quascirev.2020.106472> (2020).
26. Vettesse, D. *et al.* Neanderthal long bone breakage process: Standardized or random patterns? The example of Abri du Maras (South-eastern France, MIS 3). *J. Archaeol. Sci. Rep.* **13**, 151–163. <https://doi.org/10.1016/j.jasrep.2017.03.029> (2017).
27. Rae, A. M. & Ivanovich, M. Successful application of uranium series dating of fossil bone. *Appl. Geochem.* **1**, 419–426. [https://doi.org/10.1016/0883-2927\(86\)90026-0](https://doi.org/10.1016/0883-2927(86)90026-0) (1986).
28. Grün, R. Direct dating of human fossils. *Am. J. Phys. Anthropol.* <https://doi.org/10.1002/ajpa.20516> (2006).
29. Grün, R., Schwarcz, H. P. & Chadam, J. ESR dating of tooth enamel: Coupled correction for U-uptake and U-series disequilibrium. *Int. J. Radiat. Appl. Instrum. D Nucl. Tracks Radiat. Meas.* **14**, 237–241. [https://doi.org/10.1016/1359-0189\(88\)90071-4](https://doi.org/10.1016/1359-0189(88)90071-4) (1988).
30. St Pierre, E., Zhao, J.-X. & Reed, E. Expanding the utility of Uranium-series dating of speleothems for archaeological and palaeontological applications. *J. Archaeol. Sci.* **36**, 1416–1423. <https://doi.org/10.1016/j.jas.2009.02.004> (2009).
31. Aitken, M. J. *An Introduction to Optical Dating* (Oxford Science Publications, 1998).
32. van Klinken, G. J. Bone collagen quality indicators for palaeodietary and radiocarbon measurements. *J. Archaeol. Sci.* **26**, 687–695. <https://doi.org/10.1006/jasc.1998.0385> (1999).
33. Ambrose, S. H. Preparation and characterization of bone and tooth collagen for isotopic analysis. *J. Archaeol. Sci.* **17**, 431–451. [https://doi.org/10.1016/0305-4403\(90\)90007-R](https://doi.org/10.1016/0305-4403(90)90007-R) (1990).
34. Guiry, E. J. & Szpak, P. Improved quality control criteria for stable carbon and nitrogen isotope measurements of ancient bone collagen. *J. Archaeol. Sci.* **132**, 105416. <https://doi.org/10.1016/j.jas.2021.105416> (2021).
35. Schwarcz, H. P. & Nahal, H. Theoretical and observed C/N ratios in human bone collagen. *J. Archaeol. Sci.* **131**, 105396. <https://doi.org/10.1016/j.jas.2021.105396> (2021).
36. Galbraith, R. F., Roberts, R. G., Laslett, G. M., Yoshida, H. & Olley, J. M. Optical dating of single and multiple grains of quartz from Jimmuru rock shelter, northern Australia: Part I, experimental design and statistical models. *Archaeometry* **41**, 339–364 (1999).
37. Richards, D. A. & Dorale, J. A. in *Uranium-series geochemistry* Vol. 52 (eds B. Bourdon, G.M. Henderson, C.C. Lundstrom, & S.P. Turner) 407–460 (Reviews in Mineralogy & Geochemistry, 2003).
38. Grün, R., Eggins, S., Kinsley, L., Moseley, H. & Sambridge, M. Laser ablation U-series analysis of fossil bones and teeth. *Palaeogeography, Palaeoclimatology, Palaeoecology* **416**, 150–167. <https://doi.org/10.1016/j.palaeo.2014.07.023> (2014).
39. Crégut-Bonnouère, E., Boulbes, N., Daujeard, C., Fernandez, P. & Valensi, P. Nouvelles données sur la grande faune de l'Éémien dans le Sud-Est de la France. *Quaternaire. Revue de l'Association française pour l'étude du Quaternaire* **21**, 227–248 (2010).
40. Szmídt, C. C., Moncel, M.-H. & Daujeard, C. New data on the Late Mousterian in Mediterranean France: First radiocarbon (AMS) dates at Saint-Marcel Cave (Ardèche). *Comptes Rendus Palevol* **9**, 185–199. <https://doi.org/10.1016/j.crpv.2010.05.002> (2010).
41. Daujeard, C., Brugal, J.-P., Moncel, M.-H., Fernandes, P., Delvigne, V., Lafarge, A., Le Pape, J.-M. & Raynal, J.-P. Neanderthals and Caprines in Two Upper Pleistocene Caves of Southeastern France, in: Gourichon, L., Daujeard, C. & Brugal, J.-P. (Eds.), *Hommes et Caprinés. De la montagne à la steppe, de la chasse à l'élevage. XXXIXe rencontres internationales d'archéologie et d'histoire d'Antibes*. Éditions APDCA, Antibes, pp. 115–137 (2019).
42. Marin, J. *et al.* Neanderthal faunal exploitation and settlement dynamics at the Abri du Maras, level 5 (south-eastern France). *Quat. Sci. Rev.* **243**, 106472 (2020).
43. Sponheimer, M. *et al.* Saving old bones: A non-destructive method for bone collagen prescreening. *Sci. Rep.* **9**, 13928. <https://doi.org/10.1038/s41598-019-50443-2> (2019).
44. Fewlass, H. *et al.* Pretreatment and gaseous radiocarbon dating of 40–100 mg archaeological bone. *Sci. Rep.* **9**, 5342. <https://doi.org/10.1038/s41598-019-41557-8> (2019).
45. Ramsey, C. B., Higham, T., Bowles, A. & Hedges, R. Improvements to the pretreatment of bone at Oxford. *Radiocarbon* **46**, 155–163 (2004).
46. Wacker, L., Němec, M. & Bourquin, J. A revolutionary graphitisation system: Fully automated, compact and simple. *Nucl. Instrum. Methods Phys. Res. Sect. B Beam Interact. Mater. Atoms* **268**, 931–934. <https://doi.org/10.1016/j.nimb.2009.10.067> (2010).
47. Sýnal, H.-A., Stocker, M. & Suter, M. MICADAS: A new compact radiocarbon AMS system. *Nucl. Instrum. Methods Phys. Res. Sect. B Beam Interact. Mater. Atoms* **259**, 7–13. <https://doi.org/10.1016/j.nimb.2007.01.138> (2007).
48. Wacker, L. *et al.* MICADAS: Routine and high-precision radiocarbon dating. *Radiocarbon* **52**, 252–262. <https://doi.org/10.1017/S003822200045288> (2010).
49. Wacker, L., Christl, M. & Sýnal, H. A. Bats: A new tool for AMS data reduction. *Nucl. Instrum. Methods Phys. Res. Sect. B Beam Interact. Mater. Atoms* **268**, 976–979. <https://doi.org/10.1016/j.nimb.2009.10.078> (2010).

50. Bronk Ramsey, C. Bayesian analysis of radiocarbon dates. *Radiocarbon* **51**, 337–360 (2009).
51. Reimer, P. J. *et al.* The IntCal20 Northern Hemisphere Radiocarbon Age Calibration Curve (0–55 cal kBP). *Radiocarbon* **62**, 725–757. <https://doi.org/10.1017/RDC.2020.41> (2020).
52. Welker, F. *et al.* Palaeoproteomic evidence identifies archaic hominins associated with the Châtelperronian at the Grotte du Renne. *Proc. Natl. Acad. Sci.* **113**, 11162–11167. <https://doi.org/10.1073/pnas.1605834113> (2016).
53. van Doorn, N. L., Hollund, H. & Collins, M. J. A novel and non-destructive approach for ZooMS analysis: Ammonium bicarbonate buffer extraction. *Archaeol. Anthropol. Sci.* **3**, 281–289. <https://doi.org/10.1007/s12520-011-0067-y> (2011).
54. Buckley, M., Collins, M., Thomas-Oates, J. & Wilson, J. C. Species identification by analysis of bone collagen using matrix-assisted laser desorption/ionisation time-of-flight mass spectrometry. *Rapid Commun. Mass Spectrom.* **23**, 3843–3854. <https://doi.org/10.1002/rcm.4316> (2009).
55. R Core Team. R: A language and environment for statistical computing [R Foundation for Statistical Computing] (2021).
56. Gibb, S. & Strimmer, K. MALDIquant: A versatile R package for the analysis of mass spectrometry data. *Bioinformatics* **28**, 2270–2271. <https://doi.org/10.1093/bioinformatics/bts447> (2012).
57. Strohalm, M., Kavan, D., Novák, P., Volný, M. & Havlíček, V. mMass 3: A cross-platform software environment for precise analysis of mass spectrometric data. *Anal. Chem.* **82**, 4648–4651. <https://doi.org/10.1021/ac100818g> (2010).
58. Mercier, N. & Falguères, C. Field gamma dose-rate measurement with a NaI(Tl) detector: Re-evaluation of the “threshold” technique. *Ancient TL* **25**, 1–4 (2007).
59. Duller, G. A. Assessing the error on equivalent dose estimates derived from single aliquot regenerative dose measurements. *Ancient TL* **25**, 15–24 (2007).
60. Duller, G. A. T. Distinguishing quartz and feldspar in single grain luminescence measurements. *Radiation Measurements* **37**, 161–165 (2003).
61. Brennan, B. J., Lyons, R. G. & Phillips, S. W. Attenuation of alpha particle track dose for spherical grains. *Int. J. Radiat. Appl. Instrum. Part D Nucl. Tracks Radiat. Meas.* **18**, 249–253. [https://doi.org/10.1016/1359-0189\(91\)90119-3](https://doi.org/10.1016/1359-0189(91)90119-3) (1991).
62. Guérin, G., Mercier, N., Nathan, R., Adamiec, G. & Lefrais, Y. On the use of the infinite matrix assumption and associated concepts: A critical review. *Radiat. Meas.* **47**, 778–785. <https://doi.org/10.1016/j.radmeas.2012.04.004> (2012).
63. Guérin, G., Mercier, N. & Adamiec, G. Dose-rate conversion factors: update. *Ancient TL* **29**, 5–8 (2011).
64. Prescott, J. R. & Hutton, J. T. Cosmic ray and gamma ray dosimetry for TL and ESR. *Int. J. Radiat. Appl. Instrum. Part D Nucl. Tracks Radiat. Meas.* **14**, 223–227. [https://doi.org/10.1016/1359-0189\(88\)90069-6](https://doi.org/10.1016/1359-0189(88)90069-6) (1988).
65. Murray, A. S. & Wintle, A. G. Luminescence dating of quartz using an improved single-aliquot regenerative-dose protocol. *Radiat. Meas.* **32**, 57–73. [https://doi.org/10.1016/S1350-4487\(99\)00253-X](https://doi.org/10.1016/S1350-4487(99)00253-X) (2000).
66. Grün, R. Methods of dose determination using ESR spectra of tooth enamel. *Radiat. Meas.* **32**, 767–772. [https://doi.org/10.1016/S1350-4487\(99\)00281-4](https://doi.org/10.1016/S1350-4487(99)00281-4) (2000).
67. Yokoyama, Y., Falguères, C. & Quaegebeur, J. P. ESR dating of quartz from quaternary sediments: First attempt. *Nucl. Tracks Radiat. Meas.* **1982**(10), 921–928. [https://doi.org/10.1016/0735-245X\(85\)90109-7](https://doi.org/10.1016/0735-245X(85)90109-7) (1985).
68. Pons-Branchu, E. *et al.* A geochemical perspective on Parisian urban history based on U-Th dating, laminae counting and yttrium and REE concentrations of recent carbonates in underground aqueducts. *Quat. Geochronol.* **24**, 44–53. <https://doi.org/10.1016/j.quageo.2014.08.001> (2014).
69. Pons-Branchu, E. *et al.* U-series dating at Nerja cave reveal open system. Questioning the Neanderthal origin of Spanish rock art. *J. Archaeol. Sci.* **117**, 105120. <https://doi.org/10.1016/j.jas.2020.105120> (2020).
70. Grün, R. The DATA program for the calculation of ESR age estimates on tooth enamel. *Quat. Geochronol.* **4**, 231–232. <https://doi.org/10.1016/j.quageo.2008.12.005> (2009).
71. Grün, R. & Katzenberger-Apel, O. An alpha irradiator for ESR dating. *Ancient TL* **12**, 35–38 (1994).
72. Brennan, B. J., Rink, W. J., McGuire, E. L., Schwarcz, H. P. & Prestwich, W. V. Beta doses in tooth enamel by “one-group” theory and the ROSY ESR dating software. *Radiat. Meas.* **27**, 307–314. [https://doi.org/10.1016/S1350-4487\(96\)00132-1](https://doi.org/10.1016/S1350-4487(96)00132-1) (1997).
73. Lanos, P. & Philippe, A. Hierarchical Bayesian modeling for combining dates in archaeological context. *Journal de la Société Française de Statistique* **158**, 72–88 (2017).
74. Lanos, P. & Philippe, A. Event date model: A robust Bayesian tool for chronology building. *Commun. Stat. Appl. Methods* **25**, 131–157 (2018).
75. Lanos, P. & Dufresne, P. ChronoModel version 2.0: Software for Chronological Modelling of Archaeological Data using Bayesian Statistics (2019).

Acknowledgements

We thank the Service Régional de l’Archéologie, Auvergne-Rhône-Alpes, Ministère de la Culture for supporting fieldwork and analyses, PANOPLY (Plateforme Analytique Géosciences Paris Saclay) for the use of the MC-ICPMS at the LSCE. We thank A. Dapoigny for support with U-Th measurements (LSCE). ZooMS analyses performed in Leipzig (MPI-EVA) were financially supported by the Max Planck Society, and we thank M. Munoz-Alegre for assistance with the MALDI-TOF MS instrument (Univ. of Cambridge). Many thanks to M.J. Alonso, M. Duval, A. Medialdea and D. Moreno (CENIEH) for access to the ESR and OSL facilities at the CENIEH. V.S.-M. is supported by a Fyssen Foundation postdoctoral fellowship (2023–2025). We thank the two anonymous reviewers for their constructive comments on the manuscript.

Author contributions

Research design: M.R. and M.H.M.; Analysis: M.R., M.D.V., H.F., V.S.M., P.L., E.P.B., S.P.; Interpretation: M.R., M.H.M., M.D.V., H.F., V.S.M., P.L., E.P.B., S.P.; Supervision: M.H.M. and J.J.H.; All authors contributed to write the manuscript.

Competing interests

The authors declare no competing interests.

Additional information

Supplementary Information The online version contains supplementary material available at <https://doi.org/10.1038/s41598-024-69380-w>.

Correspondence and requests for materials should be addressed to M.R.

Reprints and permissions information is available at www.nature.com/reprints.

Publisher's note Springer Nature remains neutral with regard to jurisdictional claims in published maps and institutional affiliations.

Open Access This article is licensed under a Creative Commons Attribution 4.0 International License, which permits use, sharing, adaptation, distribution and reproduction in any medium or format, as long as you give appropriate credit to the original author(s) and the source, provide a link to the Creative Commons licence, and indicate if changes were made. The images or other third party material in this article are included in the article's Creative Commons licence, unless indicated otherwise in a credit line to the material. If material is not included in the article's Creative Commons licence and your intended use is not permitted by statutory regulation or exceeds the permitted use, you will need to obtain permission directly from the copyright holder. To view a copy of this licence, visit <http://creativecommons.org/licenses/by/4.0/>.

© The Author(s) 2024